Supplementary Information for "Assessing the Accuracy of Complex Refractive Index Retrievals from Single Aerosol Particle Cavity Ring-Down Spectroscopy"

Michael I. Cotterell,[1] Thomas C. Preston,[2] Andrew J. Orr-Ewing[1] and Jonathan P. Reid[1]*

[1] School of Chemistry, University of Bristol, Bristol, UK BS8 1TS

[2] Department of Atmospheric and Oceanic Sciences and Department of Chemistry, McGill University, 805 Sherbrooke Street West, Montreal, QC, Canada H3A 0B9

* Author for correspondence: j.p.reid@bristol.ac.uk

1. Assessing the Detection Limit in Extinction Cross Section Measurements

Our SP-CRDS measurements presented in previous publications[1–3] have largely been performed on particles with radii > 1 μm, which lie outside the accumulation mode regime of most atmospheric relevance, as well as being larger than the size of aerosol probed by conventional E-CRDS methods (typically 150 - 500 nm in radius). Here, the particle radius corresponding to the minimum detectable σ_{ext} for the 532-nm SP-CRDS instrument is determined. Our previous estimates of the minimum detectable σ_{ext} used analytical expressions commonly applied to the detection limits of spectroscopic measurements using optical cavities, and predicted that particles as small as 110 nm in radius could be probed *via* SP-CRDS.[3] However, this analysis neglected the influence of the intra-cavity standing wave on the broadening of the distribution of measured RDTs.

The numerical method presented here is more rigorous, involving the simulation of RDT data as a function of particle radius. These simulations use the parameters of our 532-nm SP-CRDS instrument in addition to typical best-estimates of the noise in measured RDTs and uncertainties in fitted particle radius. The radius corresponding to the minimum detectable change in RDT is obtained when the distribution of RDTs associated with a particle in the optical cavity is indistinguishable from the distribution for an empty cavity. Simulated RDT data were generated using the numerical method

described in Section II(*b*) of the main paper for a constant RI of $m = 1.475 + 0i$, a similar RI to those of 1,2,6-hexanetriol and glycerol – compounds which have previously been studied with the 532-nm SP-CRDS instrument.[1,2] These RDT data points were generated for a particle evaporating from a radius of 400 to 100 nm. Figure S1 plots the simulated variation in τ (red dots) with particle radius, and the corresponding variation in empty cavity RDTs, τ_0 (grey dots), assuming $\tau_0 = 25.00 \pm 0.04$ μs.

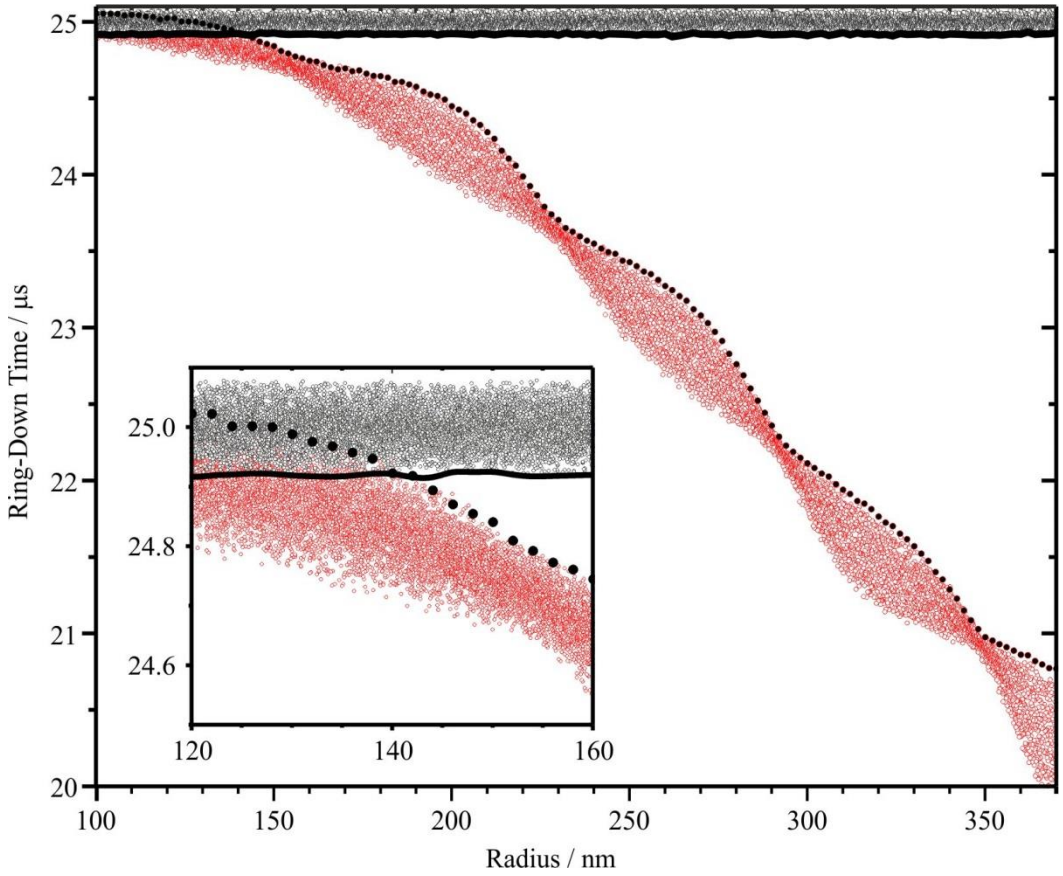

Figure S1: The variation in RDT with radius calculated from σ_{ext} simulations for a particle with $m = 1.475 + 0i$, assuming $\Delta\tau = 0.04$ μs, $\Delta a = 2$ nm, $w = 275$ μm and $L = 0.5$ m. The τ (red dots) and τ_0 (grey dots) data are shown. The solid black line represents the mean τ_0 minus two standard deviations within a 2 nm radius bin and the black dots represent the mean τ plus two standard deviations within a 2 nm radius bin.

The simulated data were analysed to determine the corresponding radius when the measured RDT was indistinguishable from the empty cavity RDTs. A conservative criterion takes the location where the upper boundary of the τ envelope crosses into the noise in τ_0. To determine this, the τ data were binned in 2 nm intervals and the mean τ plus two standard deviations was defined as the upper boundary, which is shown by the black circles in Figure S1. Similarly, a lower boundary in τ_0 was calculated as the mean τ_0 minus two standard deviations within each 2 nm bin and is shown by the black line in

Figure S1. The radius at which τ is indistinguishable from τ_0 was obtained when the black circles cross the black line, which occurred for a radius of a_{min} = 142 ± 2 nm. This particle size is well within the accumulation mode regime but is larger than the limiting radius predicted using our previous analytical method.[3] This discrepancy arises because the analytical method neglects the consequences of the cavity standing wave for the spread in τ values. The particle radius for the minimum detectable σ_{ext} will be dependent on the particle refractive index. Assuming that this particle radius scales linearly with RI, a_{min} = 157 nm for n_{532} = 1.335 (pure water), and a_{min} = 135 nm for n_{532} = 1.55 (literature RI for crystalline NaCl[4]). These values remain well within the accumulation mode regime of interest.

2. Derivation of σ_{ext} for a particle in a standing wave using GLMT

For the intra-cavity standing wave, the electric **E** field is taken to be linearly polarised in the *x*-direction and the magnetic field **H** is polarised in the *y*-direction. The **E** and **H** fields of a standing wave are described by Equation S1 and Equation S2 respectively, with *k* denoting the wavenumber in the medium, while φ is a phase factor. The time dependence of the electric and magnetic fields, $\exp(i\omega t)$, is omitted.

$$\mathbf{E}(\mathbf{r}) = \sqrt{2}E_0 \cos(kz + \varphi)\hat{\mathbf{x}} \qquad \textbf{Equation S1}$$

$$\mathbf{H}(\mathbf{r}) = -i\sqrt{2}H_0 \sin(kz + \varphi)\hat{\mathbf{y}} \qquad \textbf{Equation S2}$$

The field amplitude E_0 is related to H_0 by $E_0/H_0 = \sqrt{\mu/\epsilon}$ where ϵ is the permittivity and μ the permeability of the medium, and $\hat{\mathbf{x}}$ and $\hat{\mathbf{y}}$ are unit vectors in the Cartesian coordinate system. The factor of $\sqrt{2}$ is included in Equation S1 and Equation S2 so that the irradiance calculated using these fields will be the same as that of a travelling plane wave when averaged over a distance $\gg 2\pi/k$. For a travelling plane wave, Lorenz-Mie theory describes the scattered fields as an infinite series of spherical multipole partial waves. In GLMT, the transverse confinement of an incident beam is accounted for by multiplying each term in this series by a beam-shape coefficient.[5–9] The transverse electric $(g_l^m)_{\mathrm{TE}}$ and transverse magnetic $(g_l^m)_{\mathrm{TM}}$ beam-shape coefficients can be calculated using the two-dimensional integrals:[9]

$$(g_l^m)_{\mathrm{TE}} = \frac{-1}{4\pi}(i^{l-1})\frac{x}{j_l(x)}\frac{(l-|m|)!}{(l+|m|)!}\int_0^{2\pi}\int_0^{\pi}\left(\frac{H_{rad}(a,\theta,\phi)}{H_0}\right)P_l^{|m|}(\cos\theta)\,e^{-im\phi}\sin\theta\,d\theta d\phi \qquad \textbf{Equation S3}$$

$$(g_l^m)_{\mathrm{TM}} = \frac{-1}{4\pi}(i^{l-1})\frac{x}{j_l(x)}\frac{(l-|m|)!}{(l+|m|)!}\int_0^{2\pi}\int_0^{\pi}\left(\frac{E_{rad}(a,\theta,\phi)}{E_0}\right)P_l^{|m|}(\cos\theta)\,e^{-im\phi}\sin\theta\,d\theta d\phi \qquad \textbf{Equation S4}$$

in which E_{rad} and H_{rad} are the radial components of the incident fields, j_l are spherical Bessel functions, $P_l^{|m|}$ are associated Legendre polynomials and $x = ka$ is the size parameter at which the integrals are evaluated. It is important to note that m in these equations is an integer number and not the refractive index. When a spherical particle is centred at z_0 and φ is set to zero, Equation S1 and Equation S2 become:

$$\mathbf{E}(\mathbf{r}) = \sqrt{2}E_0\cos k(z-z_0)\hat{\mathbf{x}} \qquad \textbf{Equation S5}$$

$$\mathbf{H}(\mathbf{r}) = -i\sqrt{2}H_0\sin k(z-z_0)\hat{\mathbf{y}} \qquad \textbf{Equation S6}$$

The radial components of these fields are:

$$E_{rad} = \sqrt{2}E_0\cos k(z-z_0)\sin\theta\cos\phi \qquad \textbf{Equation S7}$$

$$H_{rad} = -i\sqrt{2}H_0\sin k(z-z_0)\sin\theta\sin\phi \qquad \textbf{Equation S8}$$

Evaluating Equation S3 and Equation S4, using these radial fields, gives:

$$(g_l^m)_{\mathrm{TE}} = -\frac{m}{\sqrt{2}}(-1)^l i^{l+1}\cos\left(kz_0+\frac{\pi l}{2}\right) \qquad \textbf{Equation S9}$$

$$(g_l^m)_{\mathrm{TM}} = \frac{1}{\sqrt{2}}(-1)^l i^{l+1}\sin\left(kz_0+\frac{\pi l}{2}\right) \qquad \textbf{Equation S10}$$

for $|m| = 1$, while for $|m| \neq 1$ the beam shape coefficients are equal to zero. The extinction cross section is then given by:

$$\sigma_{ext} = \frac{4\pi}{k^2}\mathrm{Re}\left(\sum_{l=1}^{\infty}\sum_{m=-l}^{l}\frac{2l+1}{l(l+1)}\frac{(l+|m|)!}{(l-|m|)!}(a_l|(g_l^m)_{\mathrm{TM}}|^2 + b_l|(g_l^m)_{\mathrm{TE}}|^2)\right) \qquad \textbf{Equation S11}$$

in which a_l and b_l are the usual Mie theory scattering coefficients as described in Ref. [10]. For completeness, the scattering cross section is given by:

$$\sigma_{sca} = \frac{4\pi}{k^2}\sum_{l=1}^{\infty}\sum_{m=-l}^{l}\frac{2l+1}{l(l+1)}\frac{(l+|m|)!}{(l-|m|)!}(|a_l|^2|(g_l^m)_{\mathrm{TM}}|^2 + |b_l|^2|(g_l^m)_{\mathrm{TE}}|^2) \qquad \textbf{Equation S12}$$

In computational calculations, the infinite series in Equation S11 and Equation S12 are truncated at the integer closest to $x + 4x^{1/3} + 2$.

3. Validating CSW-GLMT against Mie and CSW-Mie theory

Figure S2(a) shows a CSW-GLMT simulation of the variation of σ_{ext} with radius for a particle with a complex refractive index of $m = 1.475 + 0i$ located half-way between a node and anti-node of the 532-nm intra-cavity standing wave ($kz_0 = \pi/4$, blue line). As expected, this simulation agrees exactly with the travelling wave Mie theory prediction (red points) that was simulated using MiePlot.[11] The corresponding σ_{ext} plots for the particle centred at a node ($kz_0 = \pi/2$) and anti-node ($kz_0 = 0$) are also shown (black lines) forming the characteristic envelope representing limiting values in the σ_{ext} measurements. For $\kappa = 0$, the results of the newly developed CSW-GLMT code agree exactly with the predictions of the CSW Mie theory that has been used throughout this paper.[12]

Figure S2(b) demonstrates exact agreement between the CSW-GLMT prediction of σ_{ext} for an absorbing ($m = 1.475 + 0.1i$, blue squares) sphere located at $kz_0 = \pi/4$ and the travelling wave Mie theory prediction from MiePlot (black line). The figure includes an expanded portion of the corresponding data from Figure S2(a) for a non-absorbing particle. The fine ripple structure evident for the non-absorbing particle is damped by the effects of absorption, and a smooth monotonic increase in σ_{ext} is observed for particles with $\kappa = 0.1$.

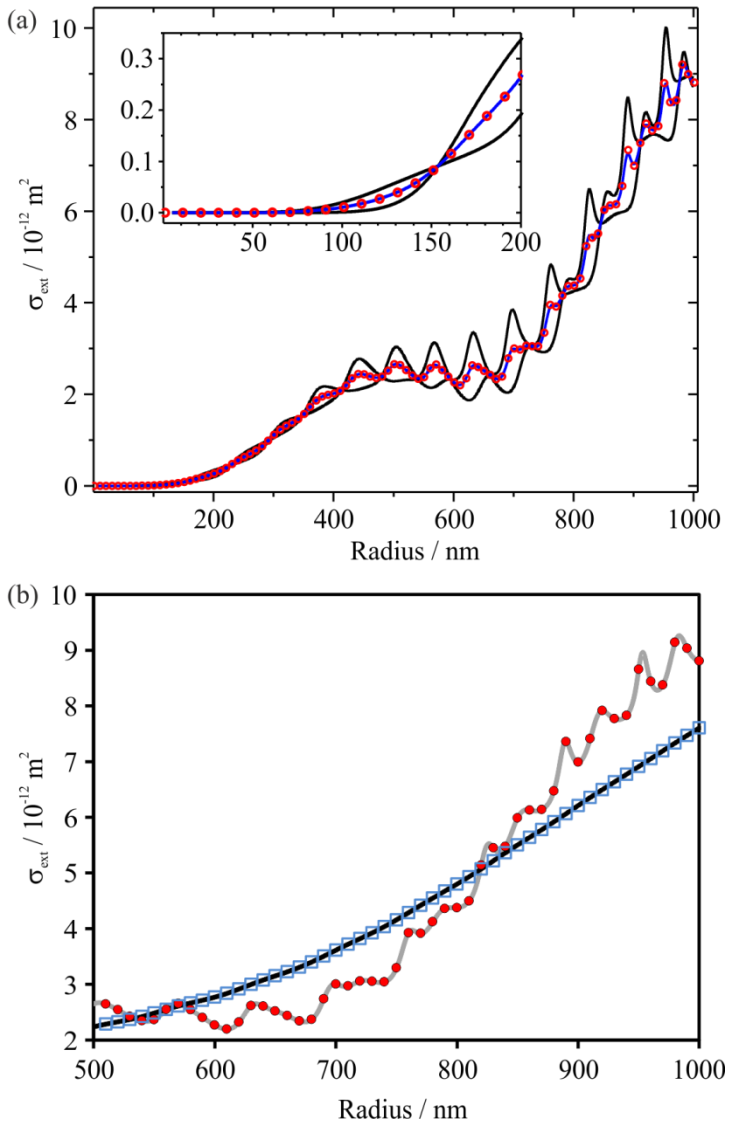

Figure S2: (a) Simulation of σ_{ext} for a particle with m = 1.475 + 0i located in a standing wave at a phase of kz_0 = $\pi/4$ (blue line) as predicted using CSW-GLMT, with a comparison to the expected σ_{ext} from traditional Mie theory (red circles). Also shown are the corresponding CSW-GLMT simulations of σ_{ext} for the particle centred at a node (kz_0 = 0) and anti-node (kz_0 = $\pi/2$) of a standing wave (black lines). (b) CSW-GLMT prediction for σ_{ext} for a non-absorbing (m=1.475+0i, red points) and absorbing (m=1.475+0.1i, blue squares) particle located in a standing wave with kz_0=$\pi/4$. The grey and black lines represent traditional Mie theory simulations for particles with RIs of m=1.475+0i and m=1.475+0.1i respectively.

References

1 B. J. Mason, M. I. Cotterell, T. C. Preston, A. J. Orr-Ewing and J. P. Reid, *J. Phys. Chem. A*, 2015, **119**, 5701–5713.

2 M. I. Cotterell, B. J. Mason, T. C. Preston, A. J. Orr-Ewing and J. P. Reid, *Phys. Chem. Chem. Phys.*, 2015.

3 M. I. Cotterell, T. C. Preston, B. J. Mason, A. J. Orr-Ewing and J. P. Reid, *Proc. SPIE*, 2015, **9548**.

4 O. B. Toon, J. B. Pollack and B. N. Khare, *J. Geophys. Res.*, 1976, **81**, 5733–5748.

5 G. Gouesbet, B. Maheu and G. Grehan, *J. Opt. Soc. Am. A*, 1988, **5**, 1427–1443.

6 J. A. Lock and G. Gouesbet, *J. Quant. Spectrosc. Radiat. Transf.*, 2009, **110**, 800–807.

7 G. Gouesbet, J. A. Lock and G. Gréhan, *J. Quant. Spectrosc. Radiat. Transf.*, 2011, **112**, 1–27.

8 G. Gouesbet and J. A. Lock, *J. Opt. Soc. Am. A*, 1994, **11**, 2516.

9 J. A. Lock and G. Gouesbet, *J. Opt. Soc. Am. A*, 1994, **11**, 2503.

10 C. F. Bohren and D. R. Huffman, *Absorption and Scattering of Light by Small Particles*, New York: Wiley, 1998.

11 P. Laven, *http://www.philiplaven.com/mieplot.htm*.

12 J. L. Miller and A. J. Orr-Ewing, *J. Chem. Phys.*, 2007, **126**, 174303.